Journal of ELECTRONIC MATERIALS, Vol. 48, No. 8, 2019
https://doi.org/10.1007/s11664-019-07261-z

Effect of Magnetic Phase on Structural and Multiferroic Properties of $Ni_{1-x}Zn_xFe_2O_4/BaTiO_3$ Composite Ceramics

YUZE XUE,[1,2] RUICHENG XU,[1,2] ZHENHUA WANG,[1,2] RONGLI GAO,[1,2,3] CHUNYUE LI,[1,2] GANG CHEN,[1,2] XIAOLING DENG,[1,2] WEI CAI,[1,2] and CHUNLIN FU[1,2,4]

1.—School of Metallurgy and Materials Engineering, Chongqing University of Science and Technology, Chongqing 401331, China. 2.—Chongqing Key Laboratory of Nano/Micro Composite Materials and Devices, Chongqing 401331, China. 3.—e-mail: gaorongli2008@163.com. 4.—e-mail: chlfu@126.com

$Ni_{1-x}Zn_xFe_2O_4/BaTiO_3$ (x = 0.3, 0.4, 0.5, 0.6, and 0.7) magnetoelectric composite ceramics have been prepared by combining the coprecipitation and sol–gel methods, and their structural and multiferroic properties studied and compared. The results indicate that the synthesized composites present biphase and composite structure, with no evident impurities observed. The lattice of the $Ni_{1-x}Zn_xFe_2O_4$ crystal structure is distorted owing to the incorporation of Zn^{2+} ions. The samples present irregular microstructure and abnormal grain growth, which can be attributed to the heterogeneous distribution of the ferroelectric and magnetic phases during preparation. The chemical composition of the larger grains is $Ni_{1-x}Zn_xFe_2O_4$, while that of the smaller grains is proven to be $BaTiO_3$. The dielectric constant of the ceramics first increases then decreases as the Zn^{2+} ion content is increased, which is related to the irregular microstructure of the ceramics. Both the frequency dependence of the dielectric loss and the temperature dependence of the dielectric constant present two relaxation peaks for all samples. The dielectric loss peaks are attributed to the slow polarization process, such as turning-direction and space-charge polarization, while the dielectric constant peaks can be ascribed to the ferroelectric phase transition of $BaTiO_3$ and relaxation polarization of the composites. The abnormal magnetization behaviors can be induced by the A–B superexchange interaction caused by the addition of nonmagnetic Zn^{2+} ions.

Key words: Multiferroic, magnetoelectric properties, magnetoelectric structure, ceramic

INTRODUCTION

Multiferroics, which simultaneously present magnetic and ferroelectric orders, have attracted great attention over recent decades owing to their novel physical properties, such as the magnetoelectric (ME) effect, and their potential applications in magnetic sensors, new capacitors, microelectromechanical systems, spintronic devices, and energy harvesters.[1–3] Among these materials, single-phase multiferroic $BiFeO_3$ is the most extensively investigated owing to its high Curie and Néel temperatures ($T_C \approx 1100$ K and $T_N \approx 640$ K, respectively), robust ferroelectricity ($P_r \approx 100$ $\mu C/cm^2$), relatively small bandgap (~ 2.7 eV), and lead-free nature.[4–8] From the perspective of practical applications, further enhancement of the multiferroic properties is one of most important challenges faced by researchers, but the weak magnetization of $BiFeO_3$ has limited its practical applications.[9,10] Nevertheless, this limitation may not exist in multiphase composite multiferroic materials, which take

(Received May 25, 2018; accepted April 30, 2019; published online May 14, 2019)

advantage of the specific coupling between their individual components. Therefore, many interesting and novel properties can be obtained that are not otherwise observed for the individual constituent phases. The ME effect in multiphase composites is generally considered to result from the magnetostrictive effect in the magnetic component and the piezoelectric effect in the ferroelectric phase. Based on this mechanism, it can be speculated that the most feasible approach for obtaining a strong ME effect is to couple the interfacial strain between the two phases by improving their magnetostrictive and piezoelectric coefficients. Therefore, it has been concluded that the magnetostrictive and piezoelectric coefficients directly influenced the ME effect, and thus that this coupling effect depends greatly on the properties of the components. To date, several composites have been analyzed, combining different doped or undoped ferroelectrics, including $Ba(Zr,Ti)O_3$, $BiFeO_3$, $Pb(Zr,Ti)O_3$, and lead magnesium niobate-lead titanate with magnetic phases, such as $CaFe_2O_4$, Fe_3O_4, γ-Fe_2O_3, $CuFe_2O_4$, $MgFe_2O_4$, $CoFe_2O_4$, $(La,Sr)MnO_3$, $NiFe_2O_4$, $MnFe_2O_4$, and Terfenol-D.[11–14]

However, in addition to the intrinsic properties of the individual components, the geometric structure of the composites also significantly influences the ME effect. Vaz et al.[10] pointed out that the geometrical phase arrangements in such composites include 0–0, 0–1, 0–2, 0–3, 1–1, 1–2, 1–3, 2–2, 2–3, and 3–3, according to their dimension. Composites with 0–3 core–shell structured geometry are expected to present a stronger ME effect owing to their superior dispersivity and connectivity, thereby overcoming the drawbacks of grain boundaries, thermal expansion, etc. Therefore, 0–3-type ME composites have received a much attention in recent years. As mentioned above, the intrinsic properties of the magnetic and ferroelectric phases play crucial roles in the ME effect, making it necessary to investigate the effects of the phase components on the ME effect of 0–3 core–shell-structured composites. In the work presented herein, ferrite $Ni_{1-x}Zn_xFe_2O_4$ (NZFO), a widely used magnetic component, was applied as the magnetic phase, owing to its strong magnetostriction and high resistance, while the ferroelectric $BaTiO_3$ (BTO) served as the ferroelectric phase owing to its excellent piezoelectric properties, low dielectric loss, and lead-free chemical composition. We investigated the effect of the magnetic phase on the structural, microstructural, dielectric, ferroelectric, and magnetic properties of the resulting NZFO/BTO-based composite multiferroics.

EXPERIMENTAL PROCEDURES

$Ni_{1-x}Zn_xFe_2O_4$ (x = 0.3, 0.4, 0.5, 0.6, and 0.7) nanoparticles were prepared by chemical coprecipitation. First, stoichiometric amounts of $Ni(NO_3)_2{\cdot}6H_2O$ (99.0% purity, Sinopharm Group Co., Ltd.), $Zn(NO_3)_2{\cdot}6H_2O$ (99.0% purity, Sinopharm Group Co., Ltd.), and $Fe(NO_3)_3{\cdot}9H_2O$ (99.0% purity, Sinopharm Group Co., Ltd.) were individually dissolved in distilled water to form $Ni(NO_3)_2$, $Zn(NO_3)_2$, and $Fe(NO_3)_3$ aqueous solutions, respectively. Next, a certain amount of dilute HNO_3 (0.1 mol/L) was added to the $Ni(NO_3)_2$ solution, under constant stirring using a glass stirring rod for 5 min. Afterward, the $Ni(NO_3)_2$, $Zn(NO_3)_2$, and $Fe(NO_3)_3$ solutions were mixed and heated up to 90°C under constant stirring. Subsequently, NaOH (4 mol/L) aqueous solution was slowly added to the mixture until the pH was 12. The mixture was constantly stirred for at least 30 min until the precipitate was completely formed. Finally, the mixture was cooled down to room temperature naturally. The obtained product was thoroughly washed using dilute HNO_3 (0.1 mol/L) until the pH reached 7, then dried at 100°C for 5 h. The obtained $Ni_{1-x}Zn_xFe_2O_4$ powder was used as the magnetic phase in the ME composites. To prepare well-dispersed NZFO/BTO composite ceramics, 50 mol.% NZFO was added to 50 mol.% BTO precursor solution synthesized using the sol–gel method.

To prepare the BTO precursor solution, $Ba(CH_3COO)_2$ (99.0% purity, Sinopharm Group Co., Ltd.) and $TiCl_2H_{28}O_4$ (99.0% purity, Sinopharm Group Co., Ltd.) were used as raw materials. Acetic acid (99.0% pure, Sinopharm Group Co., Ltd.) and 2-ethoxyethanol (99.0% purity, Sinopharm Group Co., Ltd.) were used as solvents. First, $Ba(CH_3COO)_2$ was dissolved in 2-ethoxyethanol and acetic acid mixture (volume ratio 4:1) to form the Ba precursor solution. The mixture was stirred constantly, heated to 70°C, and maintained at 70°C for 30 min to ensure complete dissolution of the $Ba(CH_3COO)_2$. The Ti precursor solution was synthesized in a similar way. Next, the Ba and Ti precursor solutions were mixed and stirred constantly for 30 min to form the BTO precursor solution. The pH of the precursor solution was adjusted to 3 by adding ethanolamine (99.0% purity, Chengdu Kelong Chemical Reagent Factory), then acetylacetone (99.0% purity, Sinopharm Group Co., Ltd.) was added to the solution to control the hydrolysis rate. The concentration of the precursor solution was subsequently adjusted to be 0.3 mol/L by adding a certain amount of 2-ethoxyethanol. Finally, the prepared NZFO nanoparticles were dispersed in the BTO precursor solution under continuous stirring, and the mixture was heated to 90°C to initiate the gelation of BTO (ferroelectric phase) on the surface of the NZFO (magnetic phase) nanoparticles.

The obtained composite gel was heated at 400°C to burn out the organic solvent, then the calcined powders were ground for 8 h. Afterwards, the powder mixtures were pressed at 12 MPa and the pressure was maintained for 10 min to form pellets with diameter of 10 mm and thickness of 1 mm using liquid paraffin as binder. After the liquid paraffin was burnt off, the samples were sintered at 1100°C for 5 h. The sintered samples were carefully

polished, then thin layers of high-temperature conductive silver adhesive were pasted on both sides. Subsequently, the samples were transferred to a box-type furnace, maintained at 800°C for 30 min, and cooled naturally to room temperature. Pure NZFO and BTO powders were also synthesized for comparative crystal structure studies.

The crystalline structure of the prepared materials was confirmed using an x-ray diffractometry (XRD, SmartLab, Rigaku, Japan) instrument featuring a Cu K_α radiation source (λ = 1.5406 Å) in the 2θ range of 20° to 80°. Field-emission scanning electron microscopy (FE-SEM, S-3700N; Hitachi, Japan) and transmission electron microscopy (TEM; JEOL, JEM-2100F) were carried out to investigated the morphology, composition, and interfaces of the samples. The dielectric constant (ε_r) and dielectric loss (tan δ) were measured using an impedance analyzer (E4980A; Agilent, USA), and the dielectric constant was calculated using the equation

$$\varepsilon_r = \frac{Cd}{\varepsilon_0 S}, \quad (1)$$

where C (F), d (m), and S (m^2) are the capacitance, thickness, and diameter of the sample, respectively, and ε_0 is the permittivity of vacuum (8.85×10^{-12} F/m).

Ferroelectric hysteresis loops (P–E) and current–voltage curves (J–E) were obtained using a ferroelectric test system (TF2000; aix-ACCT Inc., Germany). Magnetic hysteresis (M–H) loops were obtained at room temperature using a vibrating-sample magnetometer (BHV-55) featuring a maximum magnetic field of ± 1.5 T.

RESULTS AND DISCUSSION

The XRD patterns of the NZFO, BTO nanoparticles, and NZFO/BTO composites are illustrated in Fig. 1. Only NZFO and BTO are observed in the XRD spectra in Fig. 1a, and further analysis indicated that, with this XRD resolution limit, no additional impurity phase peaks were observed. The diffraction peaks in Fig. 1b could be indexed to (220), (311), (400), (422), (511), and (440) reflections of NZFO, while the remaining peaks were ascribed to (110), (111), (200), (201), (211), and (220) reflections of BTO, indicating that no apparent chemical reaction occurred between the NZFO and BTO phases in the prepared composite ceramics.

The average crystalline size of the NZFO particles was evaluated using Scherrer's formula,

$$D = \frac{K\lambda}{\beta \cos\theta}, \quad (2)$$

where D (nm) is the mean crystalline size, K is Scherrer's constant (0.89), λ is the wavelength of the x-rays (0.15406 nm for the Cu K_α radiation source), β (rad) is the full-width at half-maximum of the diffraction peak, and θ (°) is the Bragg diffraction angle.

The average crystalline size of the NZFO particles (calculated from Fig. 1a) was 25.7 nm, 29.1 nm, 35.3 nm, 34.4 nm, 35.3 nm, and 38.8 nm, respectively. Although the average crystalline sizes evaluated using Eq. 2 are not accurate enough, the average sizes of the NZFO particles calculated from the XRD spectra of the NZFO/BTO composites (Fig. 1b) ranged from 15 nm to 20 nm, all being smaller than those obtained for the corresponding single-phase materials. This difference can be attributed to the intrinsic nature of the composite nanostructures, where diffusion of the NZFO nanoparticles during sintering was inhibited because each nanoparticle could be wrapped into the BTO layer during the preparation process. Thus, these NZFO particles were isolated by the BTO phase in the composite ceramics, preventing further growth of the NZFO grains.

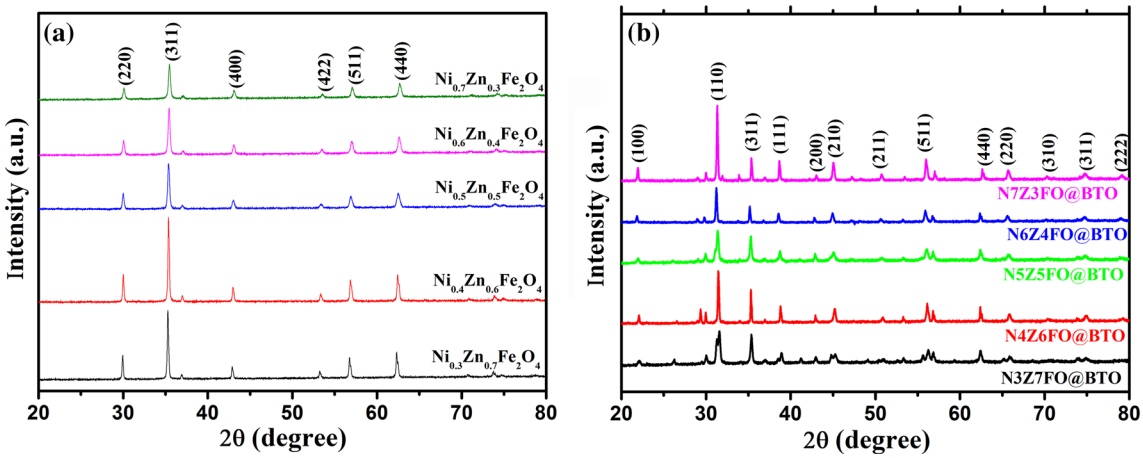

Fig. 1. x-Ray diffraction patterns of (a) pure $Ni_{1-x}Zn_xFe_2O_4$ and $BaTiO_3$ nanoparticles and (b) $Ni_{1-x}Zn_xFe_2O_4/BaTiO_3$ composite ceramics. Here, N7Z3FO, N6Z4FO, N5Z5FO, N4Z6FO, N3Z7FO, and BTO are $Ni_{0.7}Zn_{0.3}Fe_2O_4$, $Ni_{0.6}Zn_{0.4}Fe_2O_4$, $Ni_{0.5}Zn_{0.5}Fe_2O_4$, $Ni_{0.4}Zn_{0.6}Fe_2O_4$, $Ni_{0.3}Zn_{0.7}Fe_2O_4$, and $BaTiO_3$, respectively.

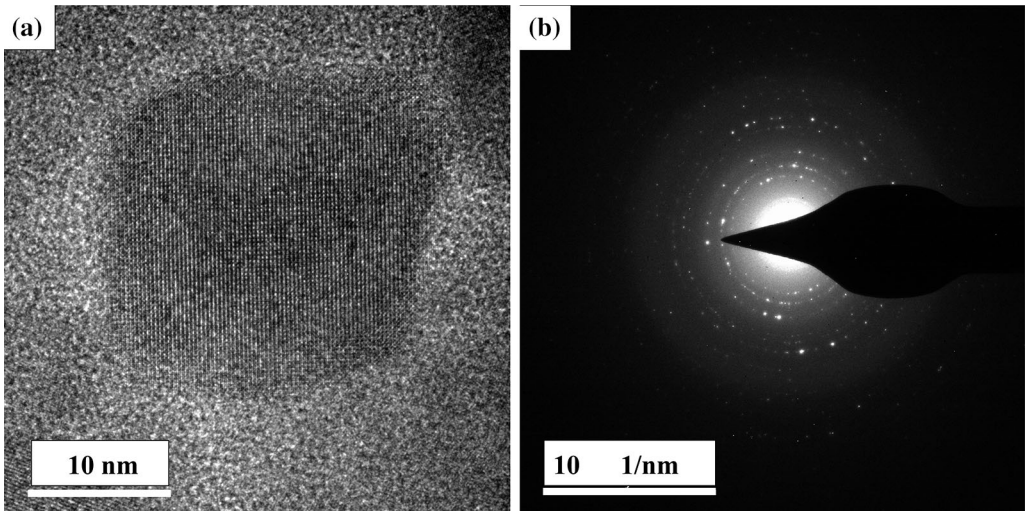

Fig. 2. (a) Typical TEM image and (b) selected-area diffraction image of $Ni_{1-x}Zn_xFe_2O_4/BaTiO_3$ composite particles.

Typical TEM images of the synthesized composite particles are depicted in Fig. 2a. A different contrast can be observed between the border and inside structure of the particles, indicating that the particles presented composite structure. In addition, nearly spherical NZFO nanoparticles with diameter of $\sim$ 22 nm can be observed. The size of the NZFO nanoparticles matched well with the XRD results in Fig. 1b and is similar to values previously reported in literature.[15] Figure 2b presents the selected-area diffraction patterns of NZFE/BTO composite particles. The particles exhibited polycrystalline structure, consistent with the XRD results. As the NZFO nanoparticles prepared using the coprecipitation method were dispersed into the BTO precursor solution, the NZFO nanoparticles acted as seeding sites for growth of NZFO/BTO ME nanocomposites.

To comparatively investigate the surface morphology of the prepared NZFO/BTO composite ceramics comprising different magnetic components, their SEM images (Fig. 3) were analyzed, revealing an uneven surface with particles of quite different sizes and shapes. Some small grains were gathered around the large grains, which could be caused by abnormal grain growth. In addition, some pores could be observed in these specimens. We hypothesize that such pores could have formed during the fast volatilization and violent combustion of the paraffin binder at high temperature, or that the adhesion offered by the paraffin binder was insufficient. In addition to the effect of the paraffin binder, the duration and pressure of the process as well as the particle size of the powder play significant roles in the formation of pores. Finally, the grain boundary between the two phases in the composites should have increased, because no obvious chemical reaction occurred between the magnetic and ferroelectric phases. Moreover, grain growth was inhibited in the ME structure, thus more grain boundary was produced. Such increased grain boundaries could induce more pores, which, in turn, could affect the properties of the samples because the generated porosity could result in low relative density. The relative density is used to estimate the density, being calculated as the ratio of the measured to theoretical density. The relative density of the $Ni_{1-x}Zn_xFe_2O_4/BaTiO_3$ ceramics was 94.8%, 93.7%, 95.4%, 94.6%, and 95.8%, with corresponding porosity of 5.2%, 6.3%, 4.6%, 5.4%, and 4.2%, for x of 0.3, 0.4, 0.5, 0.6, and 0.7, respectively.

The particles of these composites could be divided into two groups according to their size: large and small. The large grains were larger than 1 μm, while the small grains were smaller than 100 nm. We hypothesize that the compositions of the large and small grains were different, but that all the small grains presented the same composition, just as all the large grains comprised the same materials. Therefore, it was necessary to determine the chemical compositions of the large and small grains in the NZFO/BTO samples to analyze the surface microstructure, particularly the distribution of the two phases. Energy-dispersive x-ray spectroscopy (EDS) was used for this, and the results are presented in Fig. 4. Figure 4a, c reveals that the major elements present in the small grains were Ba, Ti, and O, thus these grains were considered to be BTO. Furthermore, Ni, Zn, Fe, Ti, and O were the main elements present in the large grains, as illustrated in Fig. 4b, d. Although Ti was detected in these grains, its presence can be ascribed to the large scanning range of EDS, which could have included marginal and overlapped BTO particles. Regardless of the presence of Ti, these large grains were thus mainly categorized as NZFO phase. The distribution of NZFO and BTO was relatively nonuniform, and some agglomerations were formed, which may be due to the poor dispersibility of NZFO in the BTO precursor solution (Fig. 4).

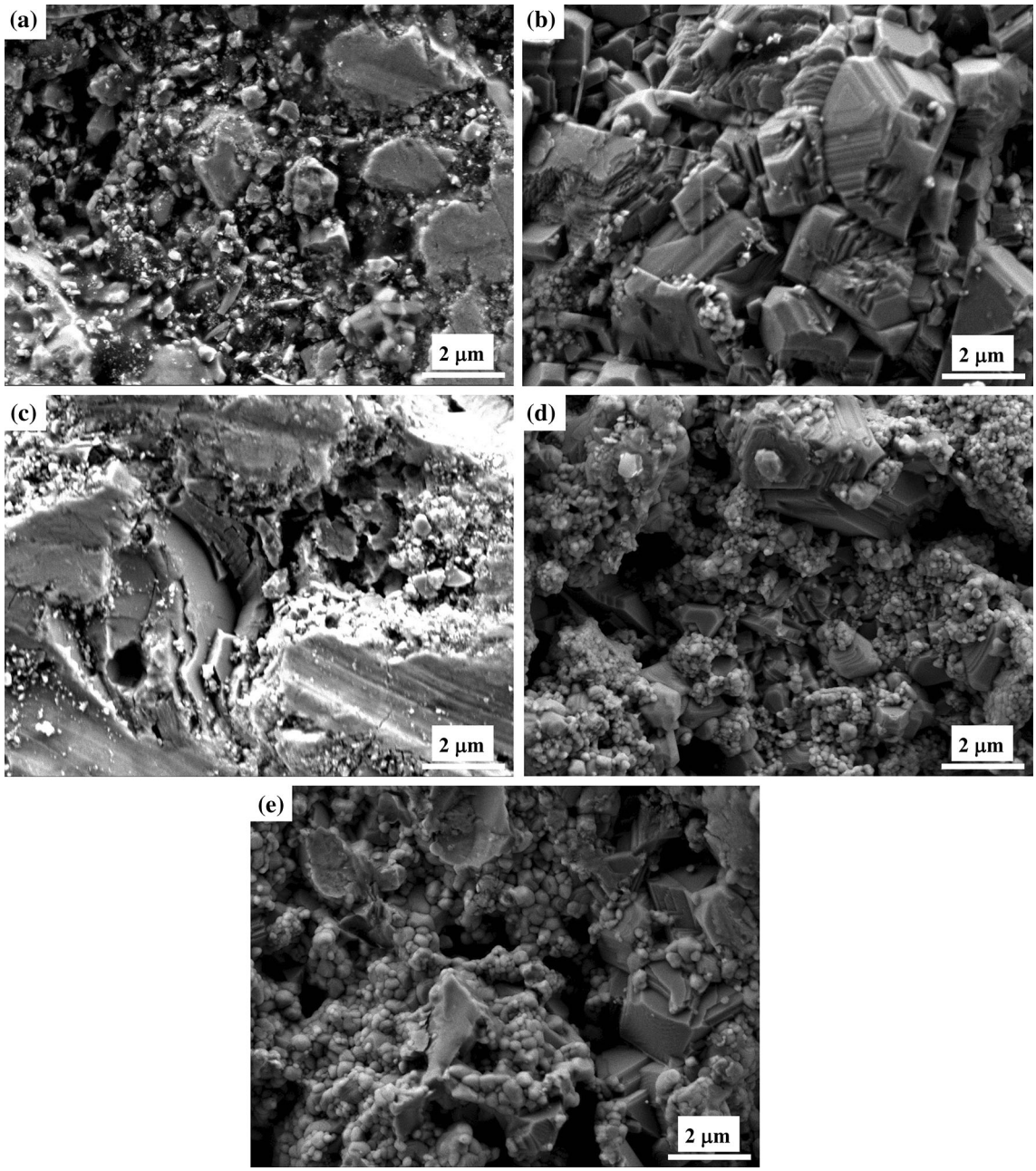

Fig. 3. SEM images of $Ni_{1-x}Zn_xFe_2O_4/BaTiO_3$ magnetoelectric structural ceramics for x of (a) 0.3, (b) 0.4, (c) 0.5, (d) 0.6, and (e) 0.7.

Figure 5 presents the room-temperature frequency (f) dependence of ε_r and $\tan\delta$ for the NZFO/BTO composite ceramics in the frequency range from 20 MHz to 20 MHz. While the ε_r values of all the composites were quite different in the low frequency region, ε_r decreased sharply as f decreased in the low frequency range. However, the ε_r values of the composites tended to be stable in the high frequency range. For the $Ni_{0.5}Zn_{0.5}Fe_2O_4/BaTiO_3$ (N5Z5FO/BTO) sample, for example, ε_r decreased from 26,000 to 1000 as f was increased from 20 Hz to 2 MHz. This decrease in ε_r can be attributed to the different polarization behaviors at different f values, and is widely described using Maxwell–Wagner theory, which assumes that the polarization of dielectric materials derives from the heterogeneous structure of the grains and corresponding grain boundaries.[15] In this study, the grain boundaries are regarded as a key factor responsible for the large ε_r values observed at low f. Temperature and/or field stress could cause free electrons to move toward grain boundaries, where they could accumulate if the resistance at the boundaries is high enough and f is low (for example, $f < 1$ kHz). Such accumulation of electrons at grain boundaries could produce polarization, resulting in the large ε_r values obtained at low f values. By contrast, when f was high, the pile-up effect of

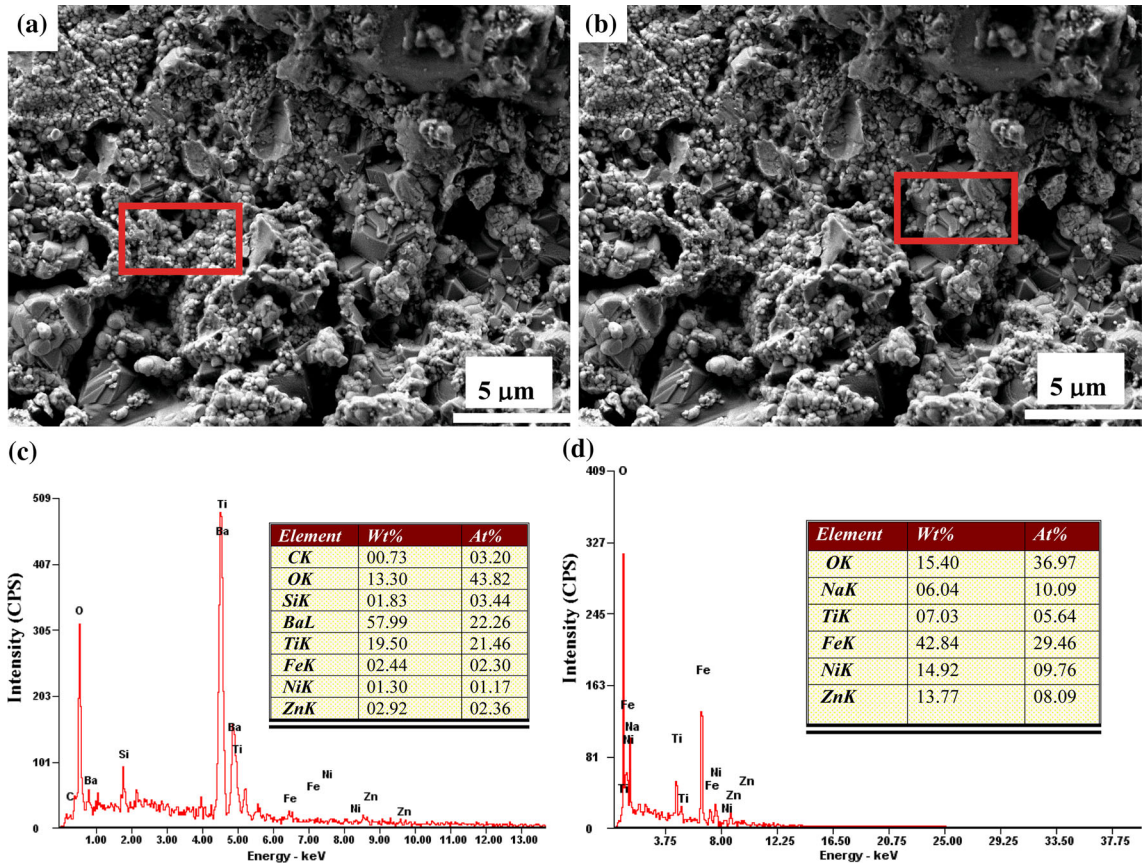

Fig. 4. Typical energy-dispersive x-ray spectroscopy images of $Ni_{1-x}Zn_xFe_2O_4/BaTiO_3$ composite ceramics in selected regions of (a, c) small and (b, d) large grains.

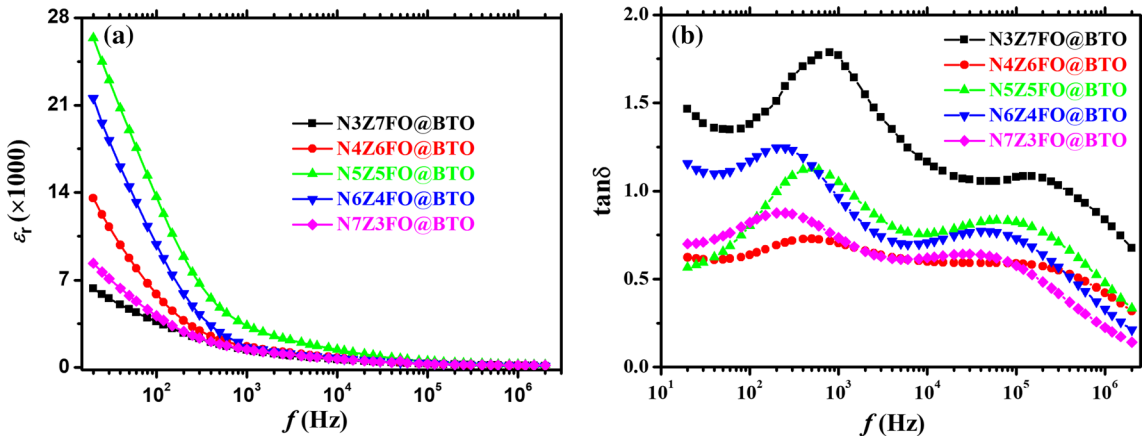

Fig. 5. Frequency (f) dependence of (a) dielectric constant (ε_r) and (b) dielectric loss (tan δ) of $Ni_{1-x}Zn_xFe_2O_4/BaTiO_3$ magnetoelectric nanocomposites (N7Z3FO, N6Z4FO, N5Z5FO, N4Z6FO, N3Z7FO, and BTO are $Ni_{0.7}Zn_{0.3}Fe_2O_4$, $Ni_{0.6}Zn_{0.4}Fe_2O_4$, $Ni_{0.5}Zn_{0.5}Fe_2O_4$, $Ni_{0.4}Zn_{0.6}Fe_2O_4$, $Ni_{0.3}Zn_{0.7}Fe_2O_4$, and $BaTiO_3$, respectively).

electrons was reduced because they kept moving back and forth, reversing their direction of movement, which decreases the polarization and thus causes ε_r to decrease. In addition, space charge is another important factor that could affect the dielectric constant at low f values, owing to the heterogeneous structure of the composites and the presence of imperfections such as impurities, porosity, and grain structure.[16] When some free charges remain at capture centers or the boundary surface of an irregular structure, they neutralize each other, forming a space-charge layer, thus the space electric field in the material may change. This generates polarization and thus increases ε_r.

The SEM and EDS results indicate that the microarchitecture of the prepared NZFO/BTO

composites was inhomogeneous, thus generating polarization and resulting in larger ε_r values at low f. As f was increased, the polarization decreased, thus ε_r decreased. At relatively high f values ($f > 10^4$ Hz), the relaxation polarization, which included the space-charge and turning-direction polarization, became very weak and only electron and ion displacement polarizations could be observed. Therefore, ε_r was small and exhibited a frequency-independent behavior, because the response time of the displacement polarization was significantly shorter than the test period, as illustrated in Fig. 5a. Hence, the dielectric properties of the composites can be explained based on the polarization mechanisms at different frequencies.

Furthermore, ε_r first increased then decreased as x, i.e., the Zn^{2+} ion content, was increased (Fig. 5a). It was expected that some Zn^{2+} ions would be incorporated into the spinel lattice, and because Zn^{2+} ions are more prone to be polarized than Ni^{2+} ions, ε_r increased as x was increased. In addition, as mentioned above, the impurities, porosity, and grain structure could increase the accumulation effect of electrons at the interface, resulting in interfacial polarization. Moreover, the grain sizes and shapes were different for the different samples (Fig. 3), which could lead to the different dielectric properties of different samples to some extent. The ε_r value of the N5Z5FO/BTO sample was the largest, exceeding 20,000 at 100 Hz.

In addition, tan δ presented nonmonotonic variation with the Zn^{2+} ion content, as illustrated in Fig. 5b. It can be speculated that, because the grain size and homogeneity differed for the different Zn^{2+} ion contents, the larger grain size implies less grain boundaries, defects, and space charges, which could result in lower tan δ values. On the other hand, the irregular grain size could lead to abnormal interactions between grains and grain boundaries, which could lead to an increase in the friction caused by domain-wall motion, thus resulting in larger tan δ values.

Although tan δ decreased overall as f was increased, all the samples presented relaxation peaks near 300 Hz and 100 kHz. These peaks could be induced by matching between the polarization and tan δ under the action of the applied electric fields at different frequencies. However, even when f reached as high as 10 MHz, such behavior was not previously reported by Verma et al.,[17] who only observed one relaxation peak at approximately 45 MHz for $Ni_{0.6}Zn_{0.4}Fe_2O_4/BaTiO_3$ (N6Z4FO/BTO) nanostructures. This difference could be explained based on the different microstructures of the composites. The slight decrease in tan δ with increasing f indicates that the dielectric dispersion followed the Maxwell–Wagner-type interfacial polarization.[17–19] Nevertheless, the resonant frequencies of the two relaxation peaks increased as the Zn^{2+} ion content was increased; For example, the first resonant frequency of the $Ni_{0.7}Zn_{0.3}Fe_2O_4/BaTiO_3$ (N7Z3FO/BTO) sample was 220 Hz, but it increased to 550 Hz for $Ni_{0.3}Zn_{0.7}Fe_2O_4/BaTiO_3$ (N3Z7FO/BTO), as illustrated in Fig. 5b. The tan δ peak is related to the free relaxation time and thus could reflect variations in the defect concentration of the doped specimens. Because the relaxation times of defects, including oxygen vacancies and space charges, are different, so were the relaxation peaks. Thus, the relaxation peaks at low f values ($\sim$ 1 kHz) can be attributed to interfacial polarization, while those at high f values ($\sim 10^5$ Hz) result from dipole orientation polarization.

Because the relaxation peaks are related to the dielectric loss mechanisms, to further elucidate the effects of inhomogeneity on the dielectric properties of the composites, the temperature dependence of ε_r was measured at 1 kHz from 300 K to 1000 K; the results are presented in Fig. 6. While ε_r generally increased as the temperature was increased, the curves for all the samples presented two peaks in the ranges of 400 K to 500 K and 800 K to 900 K. From the relationship between ε_r and the dielectric polarization, it can be hypothesized that the ε_r peak at higher temperature can be related to the phase transition of NZFO (the T_C of $NiFe_2O_4$ is approximately 865 K[20]), and that this phase-transition temperature varied with the content of Zn^{2+} ions. The ε_r peak observed at lower temperature could be the consequence of the phase transition of BTO and the mechanism of interface relaxation polarization caused by diffusion of space charges and traps.[17] This ε_r dispersion is analogous to the Maxwell–Wagner interfacial polarization, which is in agreement with Koop's phenomenological theory.

However, the location of the lower-temperature ε_r peak shifted toward lower temperature as the Zn^{2+}

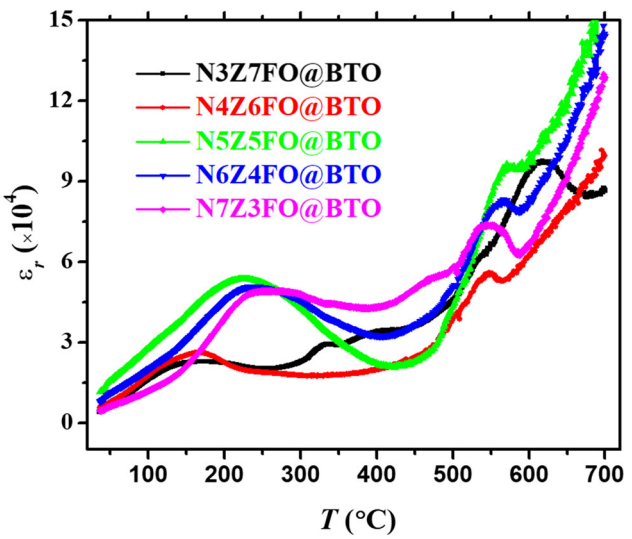

Fig. 6. Temperature (T) dependence of dielectric constant (ε_r) of $Ni_{1-x}Zn_xFe_2O_4/BaTiO_3$ composites (N7Z3FO, N6Z4FO, N5Z5FO, N4Z6FO, N3Z7FO, and BTO are $Ni_{0.7}Zn_{0.3}Fe_2O_4$, $Ni_{0.6}Zn_{0.4}Fe_2O_4$, $Ni_{0.5}Zn_{0.5}Fe_2O_4$, $Ni_{0.4}Zn_{0.6}Fe_2O_4$, $Ni_{0.3}Zn_{0.7}Fe_2O_4$, and $BaTiO_3$, respectively).

ion content was increased. When the Zn^{2+} ion content was increased from 0.3 to 0.7, the peak shifted from 538 K to 421 K, indicating that Zn^{2+} ions played an important role in the polarization mechanism of the NZFO/BTO composites. This large variation in temperature cannot be solely ascribed to the phase transition of BTO. This strong relaxation effect at lower temperature is attributed to the interfacial polarization, turning-direction polarization, and the possible contributions of hopping charge carriers along with the diffuse phase transition of ferroelectric clusters.[15,21] Among these effects, the diffuse phase transition is usually characterized by a modified Curie–Weiss law,[22]

$$1/\varepsilon - 1/\varepsilon_m = (T - T_m)^\gamma / C', \quad (3)$$

where ε and ε_m are the dielectric constant and its maximum value, respectively, T is the temperature, T_m is the temperature corresponding to ε_m, and γ and C' are constants. Here, γ reveals the character of the phase transition: $\gamma = 1$ indicates a normal ferroelectric transition, while a γ value close to 2 indicates complete ferroelectric relaxation.[22]

To investigate the relaxation behavior of the composites, the power factor, γ, was determined. Equation 3 was modified as follows:

$$\ln(1/\varepsilon - 1/\varepsilon_m) = \gamma \cdot \ln(T - T_m) + B. \quad (4)$$

The value of γ can be determined using the slope of the fitting curves of $\ln(1/\varepsilon - 1/\varepsilon_m)$ versus $\ln(T - T_m)$, as depicted in Fig. 7 and also summarized in Table I.

Although all the prepared samples were composites, γ can reveal the character of the diffuse phase transition to some extent, because the BTO component plays the dominant role in the NZFO/BTO ME composite. These fitting results indicate that γ was larger than 1 for all samples, and in particular for the N7Z3FO/BTO sample. The γ values of N6Z4FO/BTO, N5Z5FO/BTO, and $Ni_{0.4}Zn_{0.6}Fe_2O_4/BaTiO_3$ (N4Z6FO/BTO) were all close to 2, while the γ value of N7Z3FO/BTO was the largest (3.133). This can be attributed to poor crystallization of BFO, thus some amorphous phases could form at the lower sintering temperature. The presence of different internal stresses between grains could also have contributed to these results. If the grain size is very small, the internal stress can be high, thus enhancing the diffuseness of phase transitions. More importantly, the NZFO particles were coated with BTO, whose phase transition is significantly affected by interfacial stress, thus the microstructure of the composites could have influenced the dispersion phenomenon.

The dispersion phenomenon and shifting of the peaks as the Zn^{2+} ion content was changed can be attributed to compositional inhomogeneity and space-charge accumulation. The polarization of space charges presented different behaviors at different temperatures because of the inhomogeneous composition, which was affected by the porous structure and numerous grain boundaries of the NZFO/BTO composites. When electrons or space charges reach grain boundaries via hopping, if the resistance of the grain boundaries is high enough, they can accumulate at the boundaries, thereby generating polarization.[23] The microstructure of the different samples was different, thus the chances of movement and accumulation for the different samples were different even at the same temperature. Hence, the peak positions of ε_r were different for the different samples, and the peaks could be broadened in some cases. Moreover, thermally activated hopping between Fe^{2+} and Fe^{3+} ions occupying octahedral sites could induce an increase in ε_r with temperature, as could the increased movement of space charges with increasing temperature. Such charge hopping could cause a local displacement in the direction of the external applied field, thus increasing the dielectric polarization. Such dielectric behavior of the N5Z5FO/BTO nanocomposite was also reported by Curecheriu et al.[24]

To investigate the influence of the magnetic phase on the ferroelectric properties of the NZFO/BTO ceramics, room-temperature ferroelectric hysteresis loops (P–E curves) were measured at 1 kHz, as illustrated in Fig. 8a. The remanent polarization (P_r) exhibited a nonmonotonic variation with the Zn^{2+} ion content. The maximum P_r of 4.6 $\mu C/cm^2$ was found for the $Ni_{0.3}Zn_{0.7}Fe_2O_4/BaTiO_3$ (N3Z7FO/BTO) sample, while the coercive field (E_c) of this sample was also the largest, indicating that it possessed the best ferroelectric properties of all the NZFO/BTO samples in this study. Nevertheless, because of the impurities, porosity, and grain boundaries, the leakage current cannot be ignored and could strongly affect these measurement results, e.g., resulting in an overestimation of P_r and E_c.[24] In general, the larger the leakage current, the wider the P–E curves. Therefore, the values of P_r and E_c obtained from the P–E curves should be larger than the intrinsic values. To verify whether the observed larger polarization of the N3Z7FO/BTO specimen resulted from the leakage current, J–V curves of the NZFO/BTO composite ceramics were obtained at room temperature, and the results are presented in Fig. 8b.

All the composites presented large leakage current values, which are mainly related to the NZFO particles, because NZFO is a semiconductor, and its conductivity at room temperature is $\sim 10^3$ S/m, several orders of magnitude larger than that of BTO. In addition, the NZFO/BTO interfaces and pores of the samples could lead to local leakage that will reduce the resistivity of the composites. Moreover, large amounts of $Zn^{2+} \rightarrow Zn^{3+}$ and $Fe^{2+} \rightarrow Fe^{3+}$ ions were present in the material, which could have increased the leakage current density. However, very high leakage currents were observed for

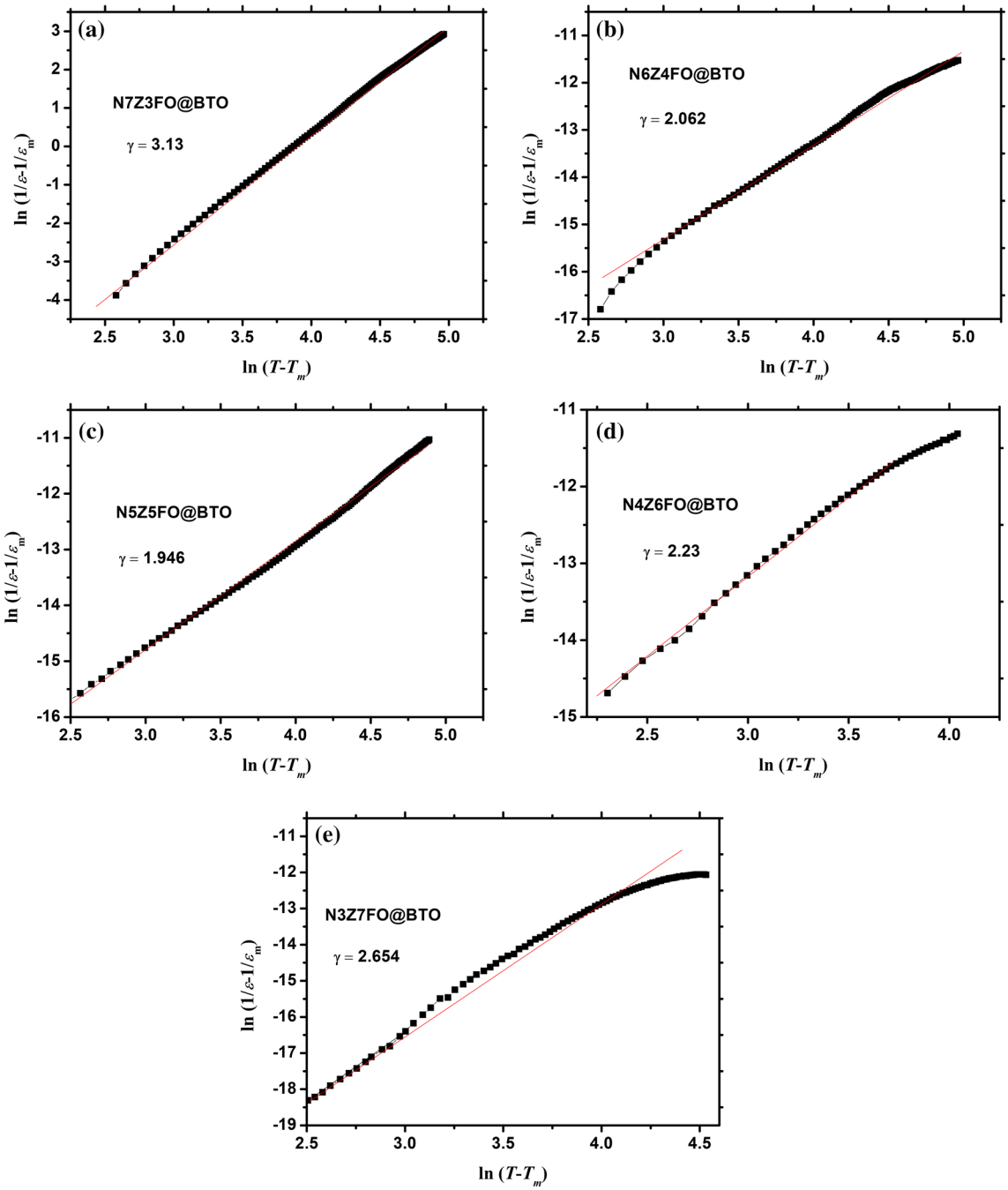

Fig. 7. $\ln(1/\varepsilon - 1/\varepsilon_m)$ versus $\ln(T - T_m)$ curves of $Ni_{1-x}Zn_xFe_2O_4/BaTiO_3$ magnetoelectric composites (ε and ε_m are the dielectric constant and its maximum value, respectively, T is the temperature, T_m is the temperature corresponding to ε_m, and N7Z3FO, N6Z4FO, N5Z5FO, N4Z6FO, N3Z7FO, and BTO are $Ni_{0.7}Zn_{0.3}Fe_2O_4$, $Ni_{0.6}Zn_{0.4}Fe_2O_4$, $Ni_{0.5}Zn_{0.5}Fe_2O_4$, $Ni_{0.4}Zn_{0.6}Fe_2O_4$, $Ni_{0.3}Zn_{0.7}Fe_2O_4$, and $BaTiO_3$, respectively).

the N4Z6FO/BTO and N5Z5FO/BTO samples. These can be ascribed to the lack of coverage of the NZFO grains by the BTO matrix, as confirmed by the SEM images in Fig. 3. In contrast, only low leakage currents were observed for the other samples, because of the isolation of the NZFO grains by the BTO matrix and/or the presence of fewer pores and increased uniformity of these samples.

Figure 9 illustrates the room-temperature magnetization versus the applied magnetic field (M–H) curves for the NZFO/BTO composites. Clear hysteresis loops can be observed, indicating typical ferromagnetic behavior with near-zero remanent magnetization (M_r) and coercive field (H_c) values, corresponding to the superparamagnetic nature of these samples. This superparamagnetic behavior can be attributed to the size effect of the NZFO particles. The NZFO particles were several tens of nanometers in size, comparable to the critical particle size, i.e., in the single-domain limit. Similar

superparamagnetic behavior has been observed for other magnetic materials such as $CoFe_2O_4$, $MnFe_2O_4$, and Fe_3O_4, prepared using the coprecipitation method.[25–28] In addition, the magnetization of all the samples saturated at approximately 1500 Oe, except for the N3Z7FO/BTO sample. The saturation magnetization, M_s, values were determined by extrapolating the M–H curve to zero applied field, and the results are listed in Table II.

The M_s value first increased then decreased as the Zn^{2+} ion content was increased. The maximum M_s value of 31.13 emu/g corresponded to N5Z5FO/BTO, while the minimal value of only 13.65 emu/g was attributed to N3Z7FO/BTO. The M_s value of 31.13 emu/g for N5Z5FO/BTO is significantly smaller than that reported for pure N5Z5FO nanoparticles by Mukherjee et al.[29] This can be attributed to the fact that the M_s value was calculated based on the total weight of the NZFO/BTO sample, even though BTO is diamagnetic. Zn^{2+} ions could affect the M_s value owing to the composite effects of large-scale cationic migration and surface spin disorder composite effects. Furthermore, the presence of BTO is likely to have affected the magnetic properties of the composites, and surface spin disorder is often associated with magnetic nanoparticles.[20] Surface spin disorder can occur due to broken or unsaturated bonds, competing interactions, or different grain boundaries. The magnetization can be increased for antiferromagnetic and ferrimagnetic nanoparticles because spin canting reduces the compensation of spins in the A and B lattices.

For an ideal spinel lattice, the magnetization is generally given by the different magnetic moments at the tetrahedral A and octahedral B sites. In $ZnFe_2O_4$, all A sites are occupied by Zn^{2+} ions and all B sites by Fe^{3+} ions. Because the magnetic moments of the Fe^{3+} ions occupying B sites are

Table I. Fitting results for T_m, $1/\varepsilon_m$, and γ of $Ni_{1-x}Zn_xFe_2O_4/BaTiO_3$ composites (ε_m, T_m, and γ are the maximum dielectric constant, temperature corresponding to ε_m, and the power factor in the modified Curie–Weiss law, while N7Z3FO, N6Z4FO, N5Z5FO, N4Z6FO, N3Z7FO, and BTO are $Ni_{0.7}Zn_{0.3}Fe_2O_4$, $Ni_{0.6}Zn_{0.4}Fe_2O_4$, $Ni_{0.5}Zn_{0.5}Fe_2O_4$, $Ni_{0.4}Zn_{0.6}Fe_2O_4$, $Ni_{0.3}Zn_{0.7}Fe_2O_4$, and $BaTiO_3$, respectively)

Sample	T_m (K)	$1/\varepsilon_m$ ($\times 10^{-5}$)	γ
N7Z3FO/BTO	526.5	2.04	3.133
N6Z4FO/BTO	505.4	1.97	2.061
N5Z5FO/BTO	496.3	1.86	1.946
N4Z6FO/BTO	438.3	4.84	2.233
N3Z7FO/BTO	428.6	4.42	2.654

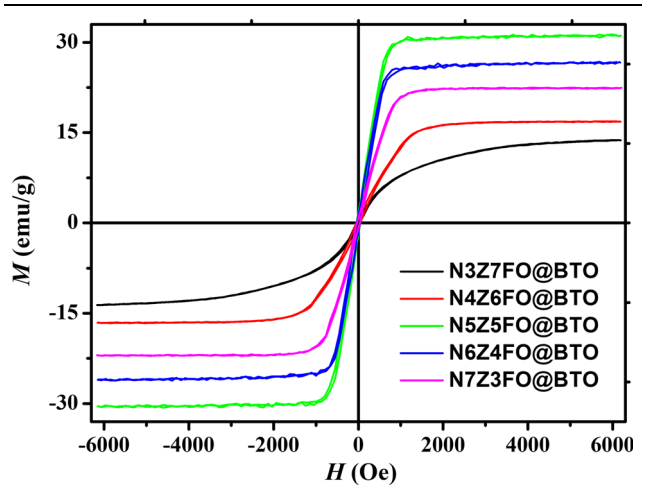

Fig. 9. Magnetic hysteresis loops of $Ni_{1-x}Zn_xFe_2O_4/BaTiO_3$ composites (N7Z3FO, N6Z4FO, N5Z5FO, N4Z6FO, N3Z7FO, and BTO are $Ni_{0.7}Zn_{0.3}Fe_2O_4$, $Ni_{0.6}Zn_{0.4}Fe_2O_4$, $Ni_{0.5}Zn_{0.5}Fe_2O_4$, $Ni_{0.4}Zn_{0.6}Fe_2O_4$, $Ni_{0.3}Zn_{0.7}Fe_2O_4$, and $BaTiO_3$, respectively).

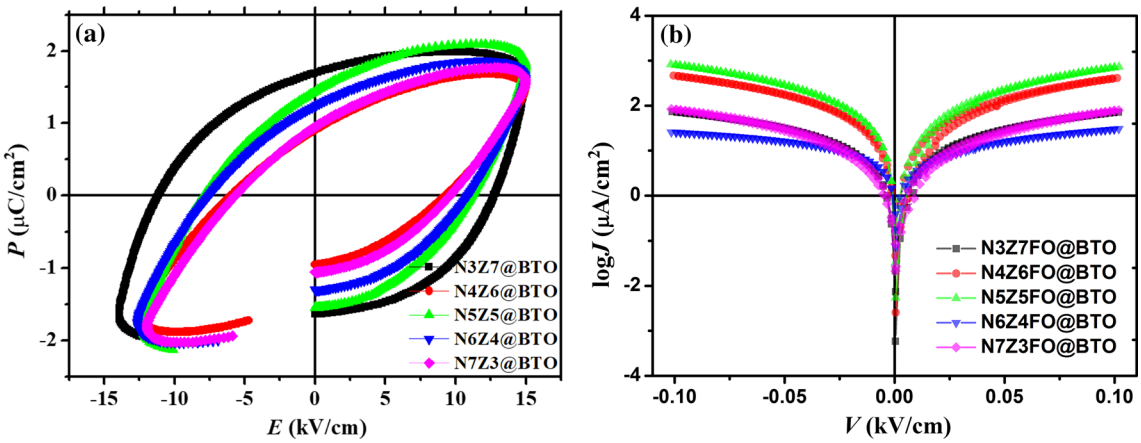

Fig. 8. (a) Ferroelectric hysteresis loops (P–E) curves and (b) current–voltage (J–V) curves of $Ni_{1-x}Zn_xFe_2O_4/BaTiO_3$ composites at 1 kHz (N7Z3FO, N6Z4FO, N5Z5FO, N4Z6FO, N3Z7FO, and BTO are $Ni_{0.7}Zn_{0.3}Fe_2O_4$, $Ni_{0.6}Zn_{0.4}Fe_2O_4$, $Ni_{0.5}Zn_{0.5}Fe_2O_4$, $Ni_{0.4}Zn_{0.6}Fe_2O_4$, $Ni_{0.3}Zn_{0.7}Fe_2O_4$, and $BaTiO_3$, respectively).

Table II. Saturation magnetization, M_s, of $Ni_{1-x}Zn_xFe_2O_4/BaTiO_3$ composites (N7Z3FO, N6Z4FO, N5Z5FO, N4Z6FO, N3Z7FO, and BTO are $Ni_{0.7}Zn_{0.3}Fe_2O_4$, $Ni_{0.6}Zn_{0.4}Fe_2O_4$, $Ni_{0.5}Zn_{0.5}Fe_2O_4$, $Ni_{0.4}Zn_{0.6}Fe_2O_4$, $Ni_{0.3}Zn_{0.7}Fe_2O_4$, and $BaTiO_3$, respectively)

Sample	N7Z3FO/BTO	N6Z4FO/BTO	N5Z5FO/BTO	N4Z6FO/BTO	N3Z7FO/BTO
M_s (emu/g)	22.33	26.52	31.13	16.74	13.65

equal in magnitude but oriented in opposite directions, they cancel each other out. Therefore, bulk $ZnFe_2O_4$ is antiferromagnetic because Zn^{2+} is nonmagnetic.[29] For the inverse spinel $NiFe_2O_4$, the Ni^{2+} ions prefer to occupy B sites,[30] while the Fe^{3+} ions are equally distributed between A and B sites. Therefore, the macroscopic magnetic properties of $NiFe_2O_4$ are determined by the magnetic moments of the Ni^{2+} ions at the B sites because the magnetic moments of the Fe^{3+} ions at the A and B sites cancel each other out. Because Ni^{2+} is a magnetic ion, $NiFe_2O_4$ presents strong magnetic properties at room temperature.

However, for the NZFO systems, although the Ni^{2+} ions are more likely to occupy B sites, the preference for A sites of the Zn^{2+} ions is so strong that some of the Fe^{3+} ions at A sites are dislocated and partly occupy B sites.[31] Therefore, the Zn^{2+} and Fe^{3+} share the A site occupancy, while the Ni^{2+} and Fe^{3+} ions are distributed at B sites. Hence, the distribution of Fe^{3+} ions at A and B sites was disturbed as the Zn^{2+} ion content was increased, reducing the compensation effect of the magnetic moments of the Fe^{3+} ions and thus increasing the macroscopic magnetization as the content of Zn^{2+} ions was increased.

The M_s value of the N5Z5FO/BTO sample was determined to be the largest, which can be attributed to the weakening of the A–B superexchange interaction due to the addition of nonmagnetic Zn^{2+} ions. Therefore, N3Z7FO/BTO exhibited paramagnetic nature and the weakest magnetization because the superexchange interaction between cations at A and B sites was absent for this sample. The magnetization of N3Z7FO/BTO did not reach saturation even at the maximum applied magnetic field of 6 kOe (Fig. 9), indicating that this sample was more difficult to magnetize.

CONCLUSIONS

$Ni_{1-x}Zn_xFe_2O_4/BaTiO_3$ composites were successfully synthesized via a coprecipitation and sol–gel approach. Formation of biphases and the ME effect was confirmed by XRD and TEM, respectively. Dispersion of the dielectric constant occurred as the amount of Zn^{2+} ions was increased, being attributed to the Maxwell–Wagner effect. The temperature dependence of the dielectric constant displayed an overall increasing trend, except for two relaxation peaks. The increasing trend was ascribed to thermal activation of space charges, while the relaxation effect was attributed to ferroelectric relaxor action and accumulation of space charges.[32] The *M–H* loops indicated ferromagnetic behavior for the composites, with a nonmonotonic increase in the saturation magnetization as the Zn content was increased. This was attributed to weakening of the A–B superexchange interaction caused by the addition of nonmagnetic Zn^{2+} ions.[33,34]

ACKNOWLEDGMENTS

This study was supported by the Natural Science Foundation of Chongqing (Grants Nos. CSTC2018jcyjAX0416, CSTC2016jcyjA0349, and CSTC2016jcyjA0175), the Young Scientific and Technological Research Program of Chongqing Municipal Education Commission (Grant No. KJQN201801509), the Program for Innovation Teams of the University of Chongqing, China (Grant No. CXTDX201601032), the Science and Technology Innovation Project of Social Undertakings and Peoples Livelihood Guarantee of Chongqing (Grant No. CSTC2017shmsA0192), the Excellent Talent Project of the University of Chongqing (Grant No. 2017-35), the Leading Talents of Scientific and Technological Innovation in Chongqing (CSTCCXLJRC201919), the Program for Technical and Scientific Innovation Led by Academician of Chongqing, the Latter Foundation Project of the Chongqing University of Science and Technology (Grant No. CKHQZZ2008002), the Scientific and Technological Achievements Foundation Project of the Chongqing University of Science and Technology (Grant No. CKKJCG2016328), and the Postgraduate Technology Innovation Project of the Chongqing University of Science and Technology (Grant No. YKJCX1720205).

REFERENCES

1. W. Eerenstein, N.D. Mathur, and J.F. Scott, *Nature* 442, 759 (2006).
2. N. Hur, S. Park, P.A. Sharma, J.S. Ahn, S. Guha, and S.W. Cheong, *Nature* 429, 392 (2004).
3. R.L. Gao, C.L. Fu, W. Cai, G. Chen, X.L. Deng, H.R. Zhang, J.R. Sun, and B.G. Shen, *Sci. Rep.* 6, 20330 (2016).
4. M.M. Saad, P. Baxter, R.M. Bowman, and J.F. Scott, *J. Phys. Condens. Matter* 16, L451 (2016).
5. R.L. Gao, Q.M. Zhang, Z.Y. Xu, Z.H. Wang, W. Cai, G. Chen, X.L. Deng, X.L. Cao, X.D. Luo, and C.L. Fu, *Nanoscale* 10, 11750 (2018).
6. G. Catalan and J.F. Scott, *Adv. Mater.* 21, 2463 (2009).
7. C.H. Yang, J. Seidel, S.Y. Kim, P.B. Rossen, P. Yu, M. Gajek, Y.H. Chu, L.W. Martin, M.B. Holcomb, Q. He, P. Maksymovych, N. Balke, S.V. Kalinin, A.P. Baddorf, S.R. Basu, M.L. Scullin, and R. Ramesh, *Nat. Mater.* 8, 485 (2009).

8. R.L. Gao, L. Bai, Z.Y. Xu, Q.M. Zhang, Z.H. Wang, W. Cai, G. Chen, X.L. Deng, and C.L. Fu, *Adv. Electron. Mater.* 4, 1800030 (2018).
9. C.A.F. Vaz, J. Hoffman, C.H. Ahn, and R. Ramesh, *Adv. Mater.* 22, 2900 (2010).
10. M. Lorenz, G. Wagner, V. Lazenka, P. Schwinkendorf, H. Modarresi, M.J. Van Bael, A. Vantomme, K. Temst, O. Oeckler, and M. Grundmann, *Appl. Phys. Lett.* 106, 012905 (2015).
11. Y. Wang and G.J. Weng, *J. Appl. Phys.* 118, 174102 (2015).
12. T. Woldu, B. Raneesh, B.K. Hazra, S. Srinath, P. Saravanan, M.V.R. Reddy, and N. Kalarikkal, *J Alloys Compd.* 691, 644 (2017).
13. A.S. Kumar, C.S.C. Lekha, S. Vivek, K. Nandakumar, and S. Nair, *J. Magn. Magn. Mater.* 418, 294 (2016).
14. R.L. Gao, Q.M. Zhang, Z.Y. Xu, Z.H. Wang, G. Chen, X.L. Deng, C.L. Fu, and W. Cai, *Compos. B* 166, 204 (2019).
15. S. Singh, N. Kumar, R. Bhargava, M. Sahni, K. Sung, and J.H. Jung, *J. Alloys Compd.* 587, 437 (2014).
16. M.A.E. Hiti, *J. Magn. Magn. Mater.* 164, 187 (1996).
17. K.C. Verma, S. Singh, S.K. Tripathi, and R.K. Kotnala, *J. Appl. Phys.* 116, 124103 (2014).
18. J.C. Maxwell, *Electricity and Magnetism* (Oxford University Press, New York, NY, 1973).
19. K.W. Wagner, *Ann. Phys.* 40, 817 (1913).
20. B. Sarkar, B. Dalal, V. Dev Ashok, and K. Chakrabarti, *J. Appl. Phys.* 115, 054421 (2014).
21. J. Hemberger, P. Lunkenheimer, R. Fichtl, H.A. Krug von Nidda, V. Tsurkan, and A. Loidl, *Nature* 434, 364 (2005).
22. K. Uchino and S. Nomura, *Ferroelectrics* 44, 55 (1982).
23. G. Sathishkumar, C. Venkataraju, and K. Sivakumar, *Mater. Sci. Appl.* 01, 19 (2010).
24. L.P. Curecheriu, M.T. Buscaglia, V. Buscaglia, L. Mitoseriu, P. Postolache, A. Ianculescu, and P.J. Nanni, *J. Appl. Phys.* 107, 104106 (2010).
25. M. Etier, C.S. Antoniak, S. Salamon, H. Trivedi, Y.L. Gao, A. Nazrabi, J. Landers, D. Gautam, M. Wintere, D. Schmitz, H. Wende, V.V. Shvartsmana, and D.C. Lupascua, *Acta Mater.* 90, 1 (2015).
26. R.L. Gao, Q.Z. Leng, Z.H. Wang, G. Chen, C.L. Fu, X.L. Deng, and W. Cai, *Mater. Res. Express.* 6, 026308 (2019).
27. J. Li, X.Y. Qiu, Y.Q. Lin, X.D. Liu, R.L. Gao, and A.R. Wang, *Appl. Surf. Sci.* 256, 6977 (2010).
28. S. Mukherjee, S. Pradip, A.K. Mishra, and D. Das, *Appl. Phys. A* 116, 389 (2014).
29. J.S. Jung, Y.K. Jung, E.M. Kim, S.H. Min, J.H. Jun, L.M. Malkinski, Y. Barnakov, L. Spinu, and K. Stokes, *IEEE Trans. Magn.* 41, 3403 (2005).
30. S. Chikazumi and S.H. Charap, *Physics of Magnetism* (Wiley, New York, 1964).
31. R. Bhargava, P.K. Sharma, A.K. Chawla, S. Kumar, R. Chandra, A.C. Pandey, and N. Kumar, *Mater. Chem. Phys.* 125, 664 (2011).
32. C.W. Nan, *Phys. Rev. B* 50, 6082 (1994).
33. R.C. Xu, Z.H. Wang, R.L. Gao, S.L. Zhang, Q.W. Zhang, Z.D. Li, C.Y. Li, G. Chen, X.L. Deng, W. Cai, and C.L. Fu, *J. Mater. Sci. Mater. Electron.* 29, 16226 (2018).
34. R.L. Gao, Z.H. Wang, G. Chen, X.L. Deng, W. Cai, and C.L. Fu, *Ceram. Int.* 44, S84 (2018).